PAPER

Check for updates

3D hollow MXene (Ti₃C₂)/reduced graphene oxide hybrid nanospheres for high-performance Li-ion storage†

Miao Guo,‡[a] Shulin Zhong,‡[a] Tian Xu,[a] Yuqin Huang,[a] Guanglin Xia, [ID][a] Tengfei Zhang [ID] *[b] and Xuebin Yu [ID] *[a]

Transition metal carbon/nitrogen compound (MXene) materials have been regarded as promising candidates for lithium-ion storage. However, two-dimensional (2D) MXenes with abundant surface functional groups easily accumulate spontaneously, which significantly reduces their specific surface area and further limits their lithium-ion storage properties. In this study, uniform three-dimensional (3D) hollow MXene nanospheres with an average diameter of < 300 nm were first synthesized *via* a template method, which used positively charged polystyrene (PS) as a template. Furthermore, reduced graphene oxide (rGO) was introduced to wrap the hollow MXene nanospheres to form hybrid MXene@rGO nanospheres. The 3D structure of the composite can not only increase the specific surface area of the material and prevent the accumulation of sheets, but also reduce the effect of volume expansion upon cycling. Meanwhile, the layer spacing between rGO and MXene sheets is only 0.26 nm, which further promotes charge exchange at the interface, so as to improve the electrochemical kinetic performance of the material. Thus, the hollow MXene@rGO nanospheres exhibited excellent rate properties as anodes for lithium-ion batteries, providing a high capacity of 241.5 mA h g⁻¹ after 5000 cycles at 10 A g⁻¹. It is demonstrated that 3D MXene@rGO nanospheres are a promising anode material for high-rate lithium-ion batteries.

1 Introduction

Since Gogotsi *et al.* discovered two-dimensional transition metal carbides and nitrides (MXenes) and first obtained a Ti₃C₂ MXene material by selectively etching Al atoms in the precursor Ti₃AlC₂ (MAX) phase with HF in 2011,[1] MXenes have attracted more and more attention.[1–7] It was demonstrated that MXene nanosheets have large interlayer channels that provide short transport paths for lithium-ion diffusion and achieve high power capability. These superior properties make them a promising material candidate for application in rechargeable lithium-ion batteries (LIBs).[8–21]

As a typical MXene, Ti₃C₂ nanosheets present good potential as a LIB anode materials in terms of experiments and theoretical calculations.[22–24] Researchers have found that the lithium-ion storage capacity of Ti₃C₂ (MXene) significantly depends on its surface functional groups.[11,13,23] The abundant functional groups such as –F, –OH, and –O on MXenes can adsorb Li⁺ and provide part of the lithium storage capacity, which makes the experimental capacity exceed the theoretical prediction capacity of Ti₃C₂. However, similar to other 2D materials, MXenes also have a propensity for "face-to-face" stacking and aggregation owing to strong van der Waals forces that hinder the ion transport, reduce the utilization of reactive sites, and increase the ion/electron transport distance, resulting in a poor rate and cycling performance. A common strategy to solve this drawback is introducing interlayer spacers, such as surfactants,[25] carbon nanotubes,[26–31] polymers,[32] and reduced graphene oxide.[33–38] However, this method can only relieve the stacking of MXene slices to a certain extent. Afterward, 2D MXenes were successfully prepared into spheres,[39] foams,[40,41] and flowers[42] using the template method, capillary assembly, and construction of MXene aerogels to reduce the contact and weaken the hydrogen bonding force between MXene sheets. Nevertheless, a three-dimensional (3D) structure can effectively promote electrolyte penetration and construct a good ion/electron transport channel, leading to high capacity and rate performance. Among these modification methods, the construction of 3D hollow spheres is the most controllable and effective. In 2017, Gogotsi *et al.* reported a method to synthesize 3D hollow MXene spheres using polymethyl methacrylate (PMMA) as a template. They were applied to a Na-ion battery to achieve good rate

ᵃDepartment of Materials Science, Fudan University, Shanghai 200433, China. E-mail: yuxuebin@fudan.edu.cn

ᵇCollege of Materials Science and Technology, Nanjing University of Aeronautics and Astronautics, Nanjing 210016, China. E-mail: zhangtengfei@nuaa.edu.cn

† Electronic supplementary information (ESI) available. See DOI: 10.1039/d1ta07250a

‡ Miao Guo and Shulin Zhong contributed equally to this work.

This journal is © The Royal Society of Chemistry 2021

J. Mater. Chem. A, 2021, **9**, 23841–23849 | 23841

performance and high cycling stability.[39] They further produced smaller 3D hollow MXene spheres using positive PS spheres as templates and then cast a homogeneous polyaniline layer onto the 3D porous MXene spheres to form an ultrafast poly-aniline@MXene cathode for high-performance asymmetric supercapacitors.[43]

As recently reported, 3D graphene frameworks are synthesized through the self-assembly of integrated graphene materials, providing significantly enhanced performance in applications in the sensing, environmental, energy, biological fields, etc.[44,45] When MXenes are combined with rGO, the synergy between the MXene and rGO can further improve the electrochemical capacity and electrochemical kinetic performance of the composite material.[46] For instance, Zhou et al.[33] constructed a 3D porous structure in a MXene/rGO hybrid film by a facile electrolyte-induced self-assembly method and used it as an anode material for LIBs. It can provide 335.5 mA h g^{-1} capacity at 50 mA g^{-1} and 100 mA h g^{-1} at 4 A g^{-1}. In addition, due to its stable structure, the film electrode has no decay in capacity after 1000 cycles at a current rate of 1 A g^{-1}, showing excellent cycling stability.

In this study, 3D hollow MXene nanospheres were first prepared via a template method, and then the surfaces of the 3D hollow MXene nanospheres were coated with a layer of reduced graphene oxide (rGO) to obtain 3D hollow MXene@rGO nanospheres with an enhanced specific surface area. The rGO acts as an electron conduction plane in the structure, which can realize fast electron transmission between the nanospheres. The excellent layer spacing of the MXene can provide a fast channel for Li$^+$ transport, which effectively improves the rate capability. Thus, the 3D hollow MXene@rGO nanospheres delivered high capacity, excellent rate performance, and stable cyclability, making the composite a promising anode material for LIBs.

2 Results and discussion

Fig. 1 shows a schematic diagram of the program to generate a 3D hollow MXene structure. The MXene flakes have negative charges due to the functional group –F on their surface, while the polystyrene (PS) spheres have positive charges due to the addition of cationic initiators in the synthesis process. As shown in Fig. S1,† the zeta potentials of the PS, MXene and GO

Fig. 1 Schematic illustration of the fabrication process of the s-MX@rGO composite.

aqueous dispersions are 17.6, −37.1 and −51.2 mV, which are consistent with ref. 47. When a delaminated Ti$_3$C$_2$T$_x$ colloidal solution was mixed with an aqueous solution of PS and stirred under ambient conditions at room temperature (RT), the film MXene (f-MX) was uniformly coated on the surface of the PS nanoparticles through electrostatic adsorption. Subsequently, the graphene oxide (GO) dispersion was added to the solution to obtain the PS@MX@GO dispersion via electrostatic adsorption. The mixed solution was then freeze-dried to obtain PS@MX@GO powder. Finally, the PS templates were removed by thermal annealing in an inert atmosphere at 500 °C, while the graphene oxide was reduced to rGO to obtain the final product. According to the different proportion of the MXene in the composite material, the spherical MXene/rGO composites (s-MX@rGO) were denoted as s-MX@rGO-1, s-MX@rGO-2 and s-MX@rGO-3 and the corresponding PS@MX@GO composites were denoted as PS@MX@Go-1, 2, and 3, respectively. To obtain spherical MXenes (s-MX) and spherical rGO (s-rGO), the MXene and GO were mixed with PS at a weight ratio of 7 : 3, respectively, and heat treated at 500 °C in an inert atmosphere. The concentrations and proportions of the precursors used in the experiment are listed in Table S1.†

The morphologies and structures of s-MX and s-MX@rGO were investigated by scanning electron microscopy (SEM) and transmission electron microscopy (TEM) characterization. The SEM images of PS@MX (Fig. 2a), PS@rGO (Fig. S2f†) and PS@MX@GO (Fig. 2b, S2d and e†) revealed that the MXene and GO nanosheets were curled and uniformly coated PS nanospheres under the action of electrostatic adsorption. After heat treatment, the 3D spherical morphology of s-MX (Fig. 2c) and s-MX@GO (Fig. 2d, S2g and h†) can be maintained well. TEM images showed that the spheres with a 250–300 nm diameter were cross-linked with each other by the MXene and rGO, presenting a hollow structure (Fig. 2f, e and S2j–l†). High-resolution transmission electron microscopy (HRTEM) showed that the shell of s-MX is mainly composed of f-MX with an interlayer distance of 1.31 nm (Fig. 2g). In contrast, the shell of s-MX@rGO is composed of the MXene with an interlayer distance of 1.31 nm and rGO with an interlayer distance of 3.4 Å (Fig. 2h, S2m and n†). Elemental mapping of s-MX@rGO by energy-dispersive X-ray spectroscopy (EDS) showed a uniform distribution in the film (Fig. 2i). It should be noted that both the MXene and rGO contain a large amount of C element. Surface scan analysis cannot directly explain why rGO is uniformly coated on the surface of the MXene ball, which needs to be analyzed in combination with the high-resolution TEM results in Fig. 2h. These results further demonstrate that the MXene and rGO coexist in the composites.

The XRD patterns of the precursors, s-MX, s-rGO and s-MX@rGO composites are shown in Fig. 3a and S3.† For s-MX@rGO with different proportions, the XRD patterns contained the characteristic peaks of both the MXene and rGO. With the decreasing content of the MXene in the s-MX@rGO composite, the intensity ratio between MXene and rGO characteristic peaks decreased, suggesting a physical mixing of the two materials. The Raman spectra in Fig. 3b show two distinct characteristic peaks of s-rGO materials, namely, the D-peak and
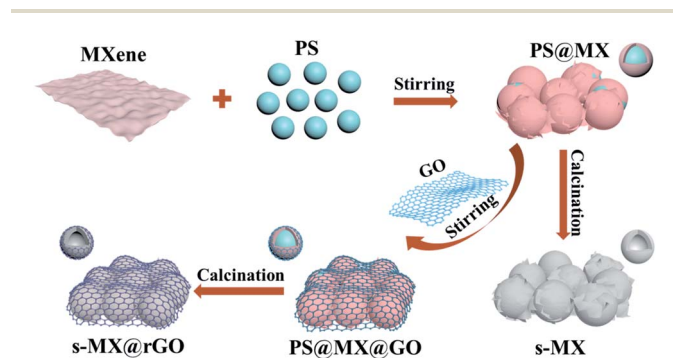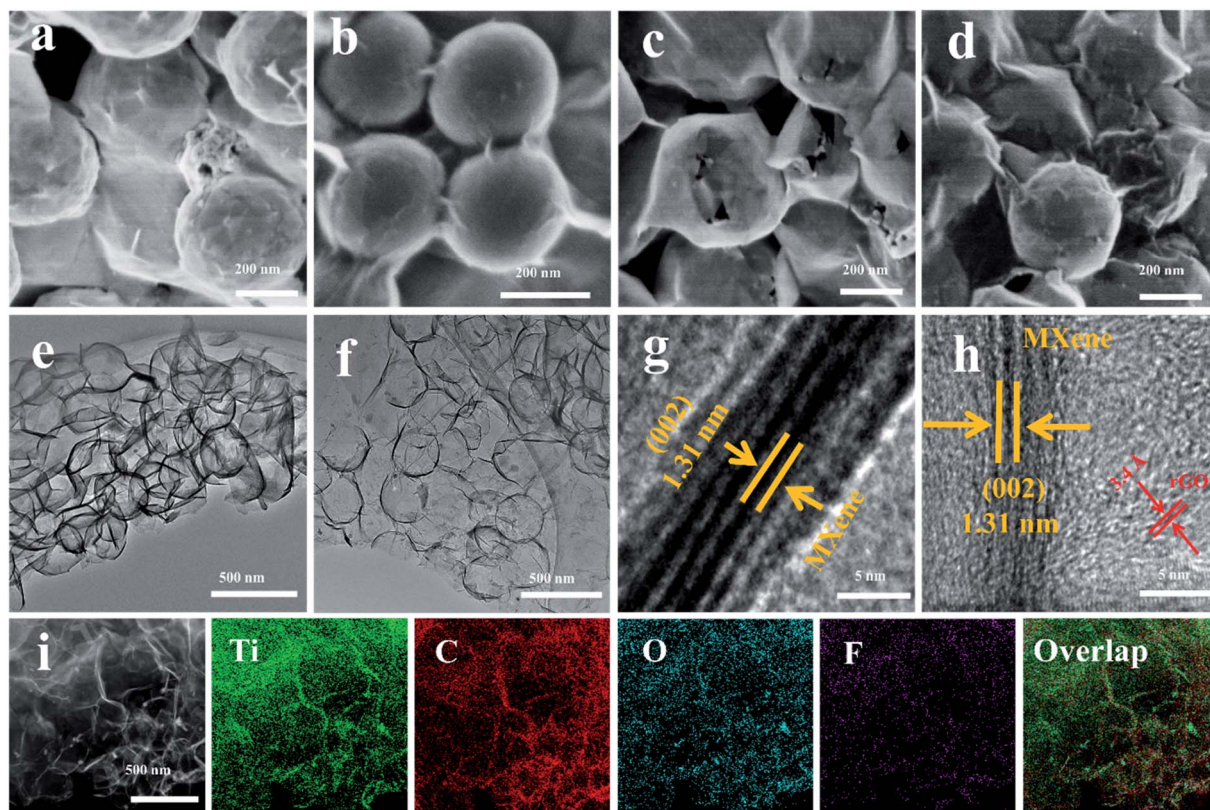
Fig. 2 SEM images of (a) PS@MX, (b) PS@MX@GO-1, (c) s-MX, and (d) s-MX@rGO-1; TEM images of (e) s-MX and (f) s-MX@rGO-1; high-resolution TEM images of (g) s-MX and (h) s-MX@rGO-1; (i) the corresponding EDS mappings of s-MX@rGO-1 of titanium (green), carbon (red), oxygen (blue), and fluorine (purple).

G-peak located at 1332 cm^{-1} and 1589 cm^{-1}, respectively. For the s-MX material, the D-peak and G-peak also exist. However, the strength of the D-peak is weak, which may be caused by the few defects of the MXene. In addition, s-MX presents two characteristic peaks of E_g at 408 cm^{-1} and 601 cm^{-1}, which are mainly caused by the mass vibration of Ti, C, and surface
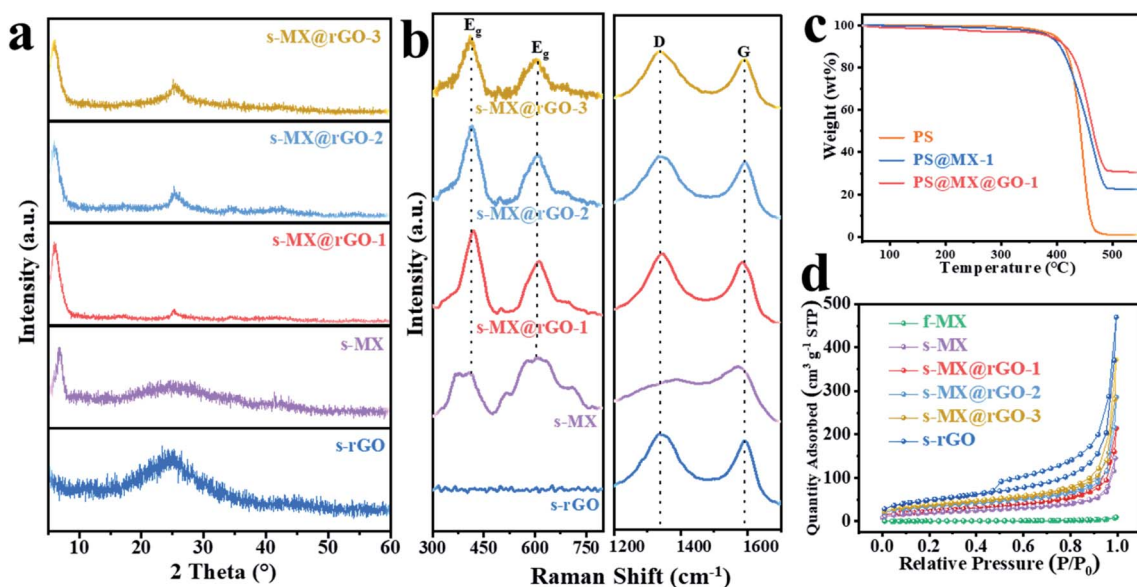

Fig. 3 (a) XRD patterns of s-MX, s-rGO, and the s-MX@rGO composite; (b) Raman spectra of s-MX, s-rGO, and the s-MX@rGO composite; (c) TGA curves of PS, PS@MX@rGO-1 and PS@MX-1; (d) BET curves of f-MX, s-MX, s-rGO, and the s-MX@rGO composite.

This journal is © The Royal Society of Chemistry 2021

J. Mater. Chem. A, 2021, 9, 23841–23849 | 23843

functional groups in the plane. When the MXene and rGO were combined, the Raman spectrum of the s-MX@rGO material was similar to that of s-MX, but the D-peak intensity increased, which confirmed the presence of rGO. Moreover, the intensity of the E_g characteristic peak belonging to the MXene decreased with a decrease in the MXene content in the s-MX@rGO composites, which is consistent with the XRD results (Fig. 3a).

TGA tests were conducted for different samples to determine the decomposition of PS and contents of the MXene and rGO in the s-MX@GO composites. The test results are shown in Fig. 3c and S4.† The PS decomposes rapidly at 450 °C and completely decomposes at 500 °C, while PS@MX-1 and PS@MX@GO-1 leave 22.7 wt% and 31 wt% products, respectively, after being decomposed at 500 °C. The content of the MXene in the obtained s-MX@rGO materials at this ratio was calculated to be 59.7 wt%, while the content of rGO was 40.3 wt%, much lower than that added in the synthesis process. The specific calculation process is shown in Fig. S4 in the ESI.† The oxygen-containing functional groups on the GO surface were removed during the reduction of GO to rGO after high temperature treatment, resulting in a large quality loss. Similarly, for s-MX@rGO-2 and s-MX@rGO-3, the content of the MXene in materials accounted for 41.1 wt% and 25.5 wt%, respectively (Fig. S4†).

The BET results in Fig. 3d show that the specific surface area of s-MX nanospheres was 69.93 m² g⁻¹ while it was only 3.62 m² g⁻¹ for f-MX, demonstrating that the 3D hollow spherical structure effectively prevented the restacking of f-MX, thus increasing the specific surface area of the MXene. The s-rGO material has the highest specific surface area (116.01 m² g⁻¹) due to the low density of rGO. Therefore, the specific surface area of s-MX@rGO can be enhanced with the introduction of rGO and increased with increasing the rGO content in the composite, reaching 86.48 m² g⁻¹, 99.42 m² g⁻¹, and 108.80 m² g⁻¹ for the s-MX@rGO-1, 2, and 3 samples, respectively.

Fig. 4a presents the cyclic voltammetry (CV) curves of the s-MX@rGO-1 composite in the first three cycles at a sweep rate of 0.1 mV s⁻¹ in the voltage range of 0.01–3.0 V *versus* Li⁺/Li. It is observed that two reduction peaks appeared at around 0.75 and 1.75 V. The reduction peak at 0.75 V is caused by the formation of a partially reversible solid electrolyte interphase (SEI) layer on the working electrode.[27,40] Another obvious reduction peak at 1.75 V was related to the lithiation of the MXene@rGO composite. The charge storage of composite materials is due to the intercalation of Li⁺ rather than a conversion reaction, so the redox peak is weak. Accordingly, in the anode curves, the oxidation peaks at 1.2 V and 2.0 V are generated by the delithiation of the MXene and rGO. These results are consistent with the charge–discharge curves (Fig. 4b). In addition, there is no other high-strength redox signal peak in the CV curves, which indicates that the lithium storage mechanism of s-MX@rGO is an intercalation reaction. The CV and charge/discharge curves of the s-MX@rGO-1 electrode in the second cycle are coincident with those of the third cycle, indicating its excellent cycling stability.

In Fig. 4c, the cycling performance of s-MX@rGO-1 with pure MXene and rGO electrodes at 100 mA g⁻¹ is compared. s-MX

provides an initial capacity of 1121.8 mA h g⁻¹ in the first cycle, which is much higher than that of f-MX (710 mA h g⁻¹). This indicates that the 3D structure of s-MX effectively prevents the stacking of lamellae, thus increasing the specific surface area of the material and providing a higher capacity during the formation of the first ring solid electrolyte film (SEI). As for the s-MX@rGO-1 electrode, it delivers outstanding discharge capacities of 1827 and 773 mA h g⁻¹ for the first and 80th cycles, comparable to those of s-rGO (1625 and 734 mA h g⁻¹) but much higher than those of pure s-Ti₃C₂ (1136 and 349 mA h g⁻¹) electrodes, indicating that the coated rGO significantly improved the electrochemical properties of s-MX at low current densities. It is worth noting that the capacity of the s-MX@rGO electrode was observed to increase after 60 cycles, which is primarily because the deintercalation of lithium ions can increase the lamellar spacing of the MXene, thus making it easier for Li⁺ to enter the reaction site. This phenomenon generally occurs in most electrodes composed of 2D materials.[33,48–50]

The rate capabilities of the s-MX@rGO composite compared with those of pure MXene and rGO electrodes are shown in Fig. 4d and S5b.† Notably, the specific capacities of s-MX@rGO-1, 2, and 3 were calculated according to the mass of the MX@rGO composite. The s-MX@rGO-1 electrode exhibited the highest reversible capacities of 659.6, 520.7, 428.4, 366.2, 318.3, and 259.7 mA h g⁻¹ at 0.1, 0.2, 0.5, 1, 2, and 5 A g⁻¹, respectively. Even when the current density was increased to 10 A g⁻¹, the s-MX@rGO-1 electrode exhibited a reversible capacity of 215.2 mA h g⁻¹. After switching the current densities back to 0.1 A g⁻¹, the s-MX@rGO-1 electrode still possessed a high reversible capacity of 659.6 mA h g⁻¹, reflecting its highly reversible characteristics. In particular, the rate performance of s-MX@rGO-1 is better than that of s-MX or s-rGO, indicating that a synergistic mechanism occurs in the s-MX@rGO composite.

The electrochemical kinetics of the s-MX@rGO composite were also demonstrated by electrochemical impedance spectroscopy (EIS). Fig. 4e shows the Nyquist plots of f-MX, s-MX, s-rGO and s-MX@rGO composite electrodes in the frequency range of 100 kHz to 0.01 Hz. The Nyquist plots of these cells have a semicircle at both high and medium frequencies and a diagonal line at low frequencies. The size of the semicircle reflects the size of the charge transmission impedance on the electrode. As observed, the s-rGO material has the lowest impedance value and the s-MX cell has the highest among these samples. Therefore, for s-MX, although the 3D hollow structure is conducive to ion transport in the electrode, the relatively low electron conductivity hinders rapid electron transport, resulting in poor multiplier performance compared with the rGO electrode. After combining with rGO, the impedance of the s-MX@rGO-1 electrode decreased, indicating that the rGO coating on s-MX enhanced the ion/electron transport rate due to the high electrical conductivity of rGO, which provides a fast channel for ion/electron transport between the nanospheres, leading to an improvement of rate performance (Fig. 4d). The method of enhancing the lithium storage performance of

23844 | *J. Mater. Chem. A*, 2021, **9**, 23841–23849

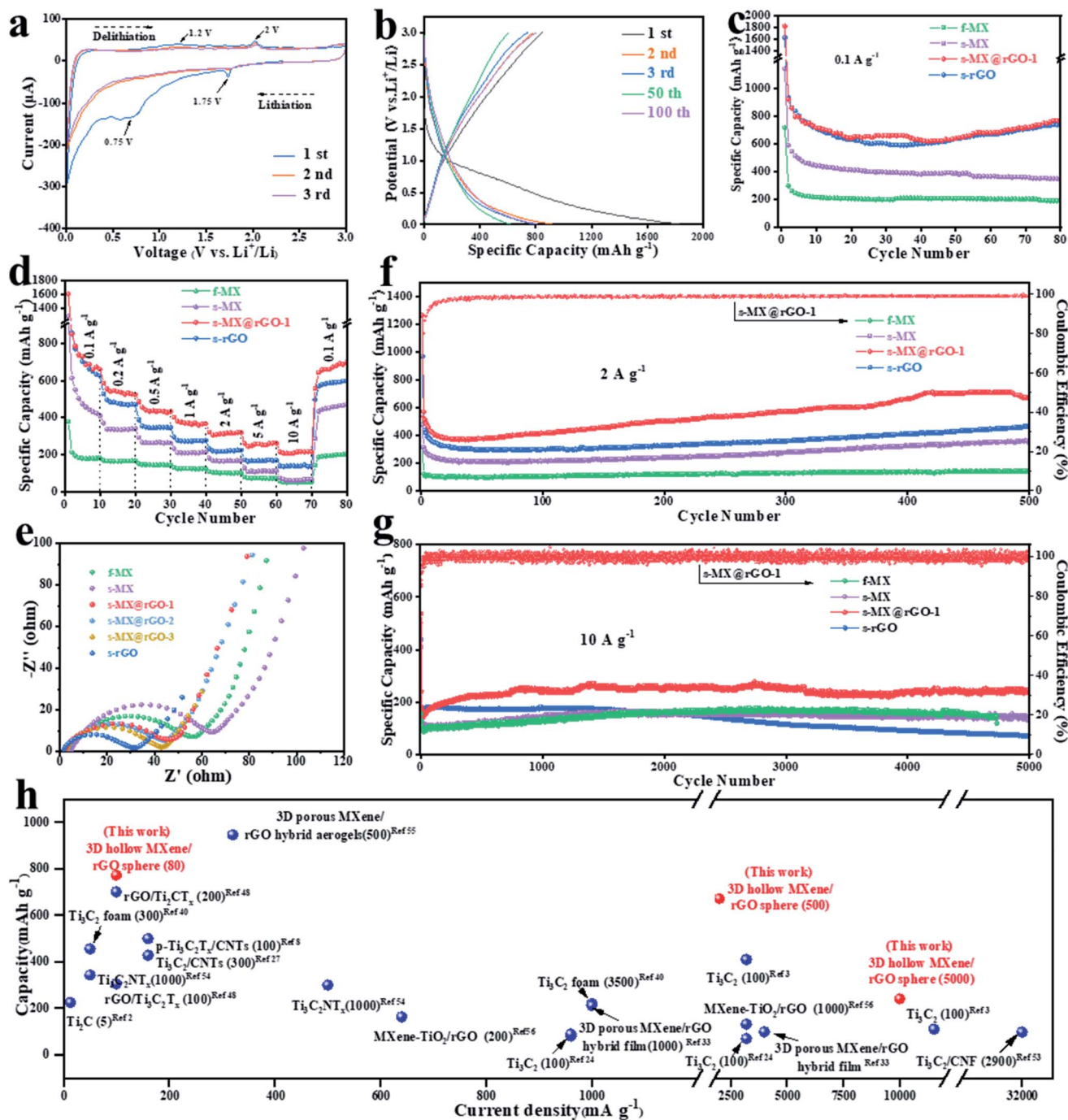This journal is © The Royal Society of Chemistry 2021

Fig. 4 Electrochemical properties of f-MX, s-MX, s-rGO, and the s-MX@rGO composites. (a) CV profiles of the s-MX@rGO-1 electrode at a scan rate of 0.1 mV s^{-1}; (b) charge/discharge curves of the s-MX@rGO-72 electrode in different cycles at 100 mA g^{-1}; (c) cycling performance of the electrodes at 100 mA g^{-1}; (d) rate capability at various current densities (0.1 A g^{-1}–10 A g^{-1}); (e) EIS plots; (f) cycling performance of electrodes at 2 A g^{-1}; (g) long-term cycling properties at 10 A g^{-1} for 5000 cycles; (h) comparison of the s-MX@rGO-1 electrode with other reported MXene-based anodes.

materials by strengthening the connections between different hollow spheres has been proved to be effective.[51,52]

The MXene, rGO, and s-MX@rGO composite electrodes were tested at high current densities of 2 and 10 A g^{-1}, respectively, to determine their cycling stability and rate performance (Fig. 4f, g, S5c and d†). The capacity of f-MX after 500 cycles was only 141.1 mA h g^{-1}. In contrast, the capacity of s-MX after 1000 cycles

reaches 354.6 mA h g^{-1}, which is much higher than that of f-MX. The improvement in the rate capability is attributed to its 3D hollow structure, which facilitates the rapid transfer of electrons and lithium ions. Significantly, s-MX@rGO-1 shows excellent long-term cycling stability with stable capacities of approximately 672.1 and 241.5 mA h g^{-1} after 500 cycles at 2 A g^{-1} and 5000 cycles at 10 A g^{-1}, respectively. The 3D hollow MXene/rGO sphere

exhibits superior electrochemical performances including high capacity, good cycling stability, and excellent rate performance in comparison with other reported MXene-based LIB anodes, such as dimethyl sulfoxide (DMSO) intercalated Ti_3C_2 powder (69 mA h g^{-1} at 2.6 A g^{-1}), delaminated f-Ti_3C_2 "paper" (110 mA h g^{-1} at 11.5 A g^{-1}), and MXene/rGO composites (98.9 mA h g^{-1} at 4 A g^{-1}) (Fig. 4h and Table S2†)[2,3,8,9,24,27,33,40,48,53–56]. To verify the relationship between excellent cycling properties and the structure of the composite material, the morphology of the cycled samples was characterized by SEM. It can be seen from Fig. S10† that the hollow nanosphere structure of s-MX@rGO can be maintained well after 100 (Fig. S6a and b†) and 500 (Fig. S6c and d†) cycles at 2 A g^{-1}. The test shows that the material has good structural stability, which explains the good cycling performance of the composite material.

CV tests on f-MX, s-MX, s-rGO, and s-MX@rGO electrodes with various ratios at different scan rates were performed to investigate the contribution of their capacitance behavior (Fig. 5, S7 and S8†). To call attention to the charge storage kinetics, an analysis of peak current (i) dependence at 2 V on the scan rate (v) was performed, based on the following relationship:

$$i = av^b. \tag{1}$$

$$\log(i) = \log(a) + b\log(v) \tag{2}$$

The value b, obtained from the slope of the curves, reflects the electrochemical behavior of the electrode material. When $b = 1$, the reaction of the electrode was completely non-diffusion-controlled. When $b = 0.5$, the reaction of the electrode was completely diffusion-controlled. Therefore, according to the value of b, the capacitive effect of the non-diffusion control and de-embedding process of diffusion control can be well identified. For the f-MX, s-MX, and s-rGO electrodes (Fig. S7†), the values of b at the cathodic peak were determined to be 0.88, 0.78, and 0.71, respectively. The results show that the lithium storage behavior of the MXene is more non-ionic diffusion-controlled than that of s-rGO, so it has a better rate performance. The b-values of the s-MX@rGO-1, 2, and 3 electrodes are 0.84, 0.76, and 0.79, respectively (Fig. 5b and S8†). Compared with pure s-MX and rGO, the b value of the composite product is improved, which shows that the electrochemical behavior of s-MX@rGO tends to be controlled by non-ionic diffusion, in agreement with their superior rate capability. The relationship between the peak current (i) and the scan rate (v) for the s-MX@rGO-1, 2, and 3 electrodes at 1.2 V also has been analyzed, and the results are shown in Fig. S9.† The b value calculated at 1.2 V is close to the b value calculated at 2 V. Therefore, we selected 2 V with more obvious peak intensity for the calculation of pseudocapacitive contribution.

The voltametric sweep rate dependence was examined more closely according to eqn (3) to quantify the contribution of capacitance and diffusion limitation to the total capacitance.
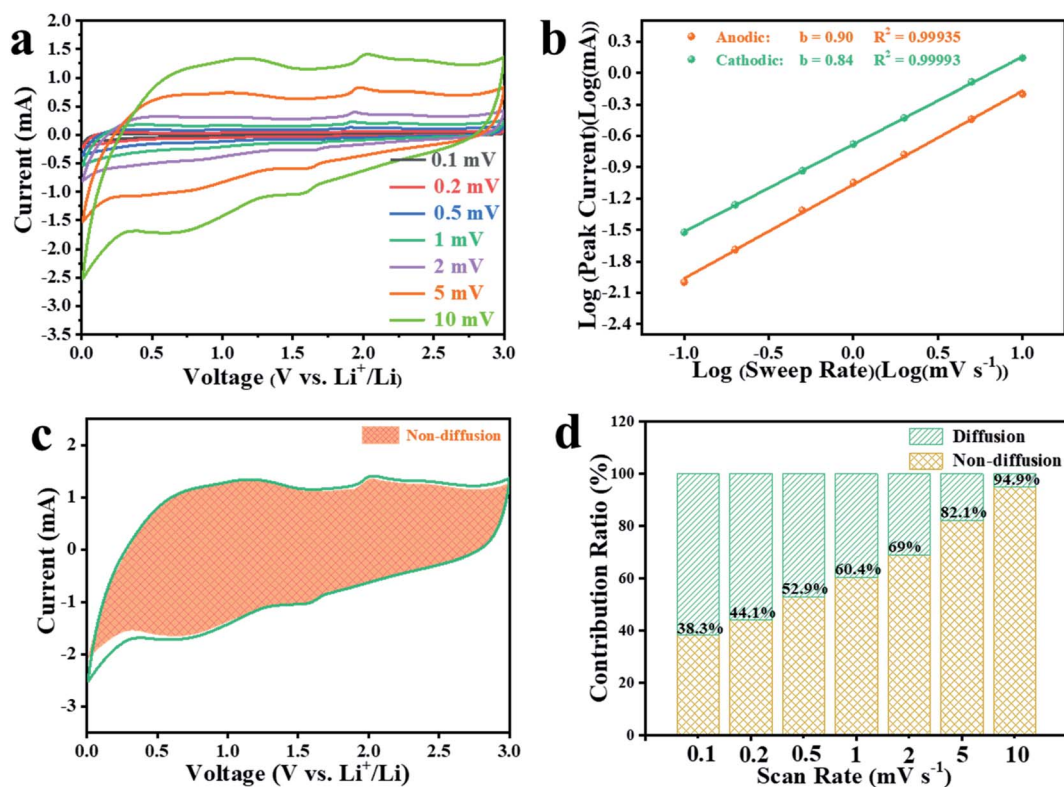

Fig. 5 (a) CV curves of the s-MX@rGO-1 electrodes at various scan rates; (b) the relationship between the peak current and scan rates from 0.1 to 10 mV s^{-1} for the s-MX@rGO-1 electrode at 2 V; (c) pseudocapacitive contribution in the CV curve of s-MX@rGO-1 at a scan rate of 10 mV s^{-1}; (d) pseudocapacitive contribution (in percentage) at different scan rates.

$$i = k_1 v + k_2 v^{1/2} \qquad (3)$$

In the formula, i is the current at a given potential, and $k_1 v$ and $k_2 v^{1/2}$ respectively correspond to the current contributions from the diffusion-controlled intercalation process and surface capacitive effect. As shown in Fig. 5c, the prevailing contribution at 10 mV s^{-1} is due to the surface capacitive effect (purple region in Fig. 5c), which contributed 94.9% of the total capacitance of the s-MX@rGO-1 electrode. The other pseudocapacitive contributions obtained were 38.3%, 44.1%, 52.9%, 60.4%, 69%, 82.1%, and 94.9% at sweep rates of 0.1, 0.2, 0.5, 1, 2, 5, and 10 mV s^{-1}, respectively (Fig. 5d). At a high scan rate, the dominant pseudocapacitive contribution leads to rapid Li$^+$ intercalation/deintercalation, which accounts for good reversibility and rate capability. The results were slightly higher than those of s-MX@rGO-2 (Fig. S8d†) and s-MX@rGO-3 (Fig. S8h†). The main reason is that the content of the MXene in s-MX@rGO-1 is the highest among these samples.

The outstanding lithium storage properties of s-MX@rGO can be attributed to the 3D hollow structure, which is beneficial for increasing the specific surface area of the material and increasing the number of reactive sites, resulting in a higher lithium storage capacity. The hollow structure is conducive to the penetration of the electrolyte, thus accelerating the transmission speed of the lithium ions. Owing to its excellent mechanical properties, the MXene can maintain its structural stability during cycling, and the addition of rGO can realize the overall enveloping of s-MX, which further promotes electronic transmission between MXene spheres. Fig. 6a schematizes the mechanism of improving the surface electron transport properties of the materials by the rGO coating. Although the pure MXene spheres were cross-linked, the contact between the spheres was not tight, which results in high resistances to electron and ion transport. After being combined with rGO, the rGO with high conductivity can coat the whole nanospheres, providing a fast channel for ion/electron transmission between nanospheres. In addition, electrons can transfer within the cathode *via* rGO instead of the poor-contacted interface between two MXene sheets (Fig. 6b), thus improving the electrochemical dynamic properties of the materials. Furthermore, the Li$^+$ diffusion coefficient of the material was calculated by using the EIS plots (Fig. S10†). The Li$^+$ diffusion coefficient of s-MX, s-rGO, and s-MX@rGO is 3.88×10^{-14}, 3.80×10^{-12} and 1.33×10^{-13} cm^2 s^{-1}, respectively. The results show that the diffusion coefficient of the pure MXene sphere of the composite material is significantly improved, which partially explains the reason for the increase in the rate performance of the s-MX@rGO composite.

To further prove the effect of rGO coating on electron conduction, DFT calculation was used to simulate the improvement of cathode performance caused by the
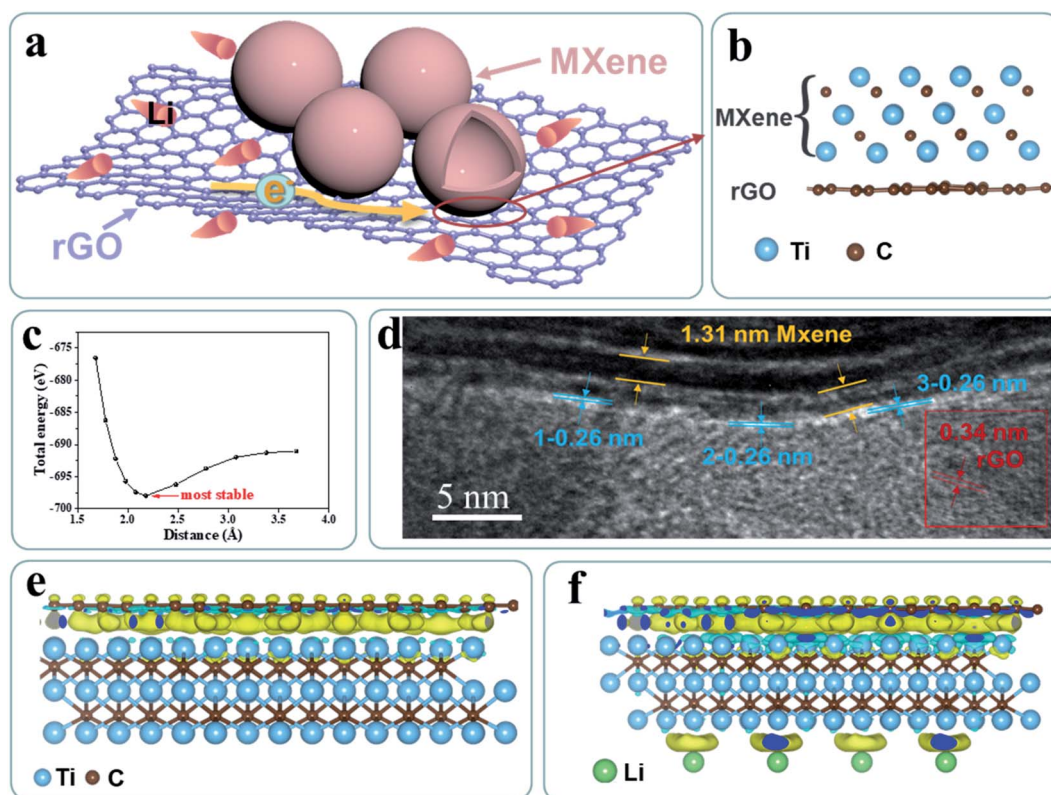

Fig. 6 (a) Mechanism schematic diagram of improving the surface electron transport properties of the materials by rGO coating. (b) Schematic diagram of the spacing between MXene and rGO layers. (c) Energy change curve with the layer spacing of the MXene and rGO. (d) High-resolution TEM images of the layer spacing of the MXene and rGO. (e) Charge density difference map of s-MX@rGO. (f) Charge density difference map of Li$^+$ s-MX@rGO.

introduction of rGO. Comparing the total energy of rGO–MXene interfaces with varied layer spacing, it is found that the most stable layer spacing is about 0.22 nm (Fig. 6c), which is much closer than the MXene–MXene interface and provides a better interface contact. The interface spacing between rGO and the MXene was well distinguished by the HRTEM image (Fig. 6d and S11†). It shows that the layer spacing of the MXene and rGO is 1.31 nm and 0.34 nm respectively, and the layer spacing at the interface is 0.26 nm, consistent with the DFT calculated results. The Li ions are mainly stored between the spacing of the MXene and rGO through an intercalation mechanism at low current charge and discharge. The distance between the MXene and rGO layer is 0.26 nm, which is very suitable for storing Li ions. Therefore, the composite material has high lithium storage capacity at a low current density.

The electronic structure of s-MX@rGO (both pristine and Li-deposited) is shown in Fig. 6e and f by analyzing the charge density difference maps. In Fig. 6e, a strong negative charge accumulation can be seen between rGO and the MXene and some small ones on the Ti and C atoms at the top of the MXene and C atoms in rGO, while positive charge accumulations are found on C–C bonds in rGO and on top Ti atoms in the MXene. Such a charge redistribution ensures a sterling contact between rGO and the MXene. After the deposition of Li, a new negative charge accumulation appears at the bottom of Li atoms, and the previous one between 2 sheets gets stronger (Fig. 6f). It indicates that electrons can transfer from Li to MXene sheets, and then to rGO. All the results given by DFT simulation prove that rGO ameliorates the electronic performance of s-MX by constructing shorter and faster paths for charge transmission. In the process of charging and discharging at a high rate, Li ions mainly adhere to the surface of the material, appearing as pseudocapacitance. The film MXene is prone to stacking resulting in a reduced specific surface area, while the spherical MXene can alleviate this stacking phenomenon, and the specific surface area is greatly increased. The BET test results also verify this. At the same time, the rGO on the surface can further improve the conductivity of the material and quickly conduct the electrons detached from the Li attached to the composite surface. These results further verify that s-MX@rGO is an ideal substrate for high-rate LIBs.

3 Conclusion

In summary, we employed a simple template method for the successful fabrication of 3D hollow MXene/rGO hybrids as anode materials for LIBs. These new hybrids exhibit high reversible capacities and excellent rate performances. A reversible capacity of 808.6 mA h g^{-1} at 0.1 A g^{-1} after 100 cycles and 672.1 mA h g^{-1} at 2 A g^{-1} after 500 cycles was achieved for s-MX@rGO-1. More importantly, the as-prepared hybrid anode material exhibits outstanding rate capability, which can reach up to 241.5 mA h g^{-1} at 10 A g^{-1} after 5000 cycles. The performance improvement is attributed to the material's 3D hollow structure, which provides a larger specific surface area and more active sites. The addition of rGO can realize the overall coating of s-MX, improve the overall electrical conductivity of

the material, and further promote electronic transmission between the MXene spheres. The method used here is facile and general and can be used to prepare other 3D structure MXene hybrids for energy storage.

Conflicts of interest

The authors declare no conflicts of interests.

References

1 M. Naguib, M. Kurtoglu, V. Presser, J. Lu, J. Niu, M. Heon, L. Hultman, Y. Gogotsi and M. W. Barsoum, *Adv. Mater.*, 2011, **23**, 4248–4253.

2 J. Come, M. Naguib, P. Rozier, M. W. Barsoum, Y. Gogotsi, P. L. Taberna, M. Morcrette and P. Simon, *J. Electrochem. Soc.*, 2012, **159**, A1368–A1373.

3 O. Mashtalir, M. Naguib, V. N. Mochalin, Y. Dall'Agnese, M. Heon, M. W. Barsoum and Y. Gogotsi, *Nat. Commun.*, 2013, **4**, 1716.

4 M. Ghidiu, M. R. Lukatskaya, M. Q. Zhao, Y. Gogotsi and M. W. Barsoum, *Nature*, 2014, **516**, 78–81.

5 J. C. Lei, X. Zhang and Z. Zhou, *Front. Phys.*, 2015, **10**, 276–286.

6 H. An, T. Habib, S. Shah, H. Gao, M. Radovic, M. J. Green and J. L. Lutkenhaus, *Sci. Adv.*, 2018, **4**, eaaq0118.

7 H. Wang, Y. Wu, X. Yuan, G. Zeng, J. Zhou, X. Wang and J. W. Chew, *Adv. Mater.*, 2018, **30**, 1704561.

8 C. E. Ren, M.-Q. Zhao, T. Makaryan, J. Halim, M. Boota, S. Kota, B. Anasori, M. W. Barsoum and Y. Gogotsi, *ChemElectroChem*, 2016, **3**, 689–693.

9 S. J. Kim, M. Naguib, M. Q. Zhao, C. F. Zhang, H. T. Jung, M. W. Barsoum and Y. Gogotsi, *Electrochim. Acta*, 2015, **163**, 246–251.

10 Y. S. Wang, Y. Y. Li, Z. P. Qiu, X. Z. Wu, P. F. Zhou, T. Zhou, J. P. Zhao, Z. C. Miao, J. Zhou and S. P. Zhuo, *J. Mater. Chem. A*, 2018, **6**, 11189–11197.

11 Y. Xie, M. Naguib, V. N. Mochalin, M. W. Barsoum, Y. Gogotsi, X. Yu, K. W. Nam, X. Q. Yang, A. I. Kolesnikov and P. R. Kent, *J. Am. Chem. Soc.*, 2014, **136**, 6385–6394.

12 Q. Tang, Z. Zhou and P. Shen, *J. Am. Chem. Soc.*, 2012, **134**, 16909–16916.

13 D. Er, J. Li, M. Naguib, Y. Gogotsi and V. B. Shenoy, *ACS Appl. Mater. Interfaces*, 2014, **6**, 11173–11179.

14 Z. J. Wang, F. Wang, K. Y. Liu, J. F. Zhu, T. R. Chen, Z. Y. Gu and S. Yin, *J. Alloys Compd.*, 2021, **853**, 157136.

15 J. Yang, W. Bao, P. Jaumaux, S. Zhang, C. Wang and G. Wang, *Adv. Mater. Interfaces*, 2019, **6**, 180224.

23848 | *J. Mater. Chem. A*, 2021, **9**, 23841–23849

This journal is © The Royal Society of Chemistry 2021

16 U. Yorulmaz, İ. Demiroğlu, D. Çakir, O. Gülseren and C. Sevik, *J. Phys.: Energy*, 2020, **2**, 032006.

17 Y. Y. Liu, J. X. Yu, D. F. Guo, Z. J. Li and Y. J. Su, *J. Alloys Compd.*, 2020, **815**, 152403.

18 X. Xu, Y. Zhang, H. Sun, J. Zhou, F. Yang, H. Li, H. Chen, Y. Chen, Z. Liu, Z. Qiu, D. Wang, L. Ma, J. Wang, Q. Zeng and Z. Peng, *Adv. Electron. Mater.*, 2021, **7**, 2000967.

19 T. Kshetri, D. T. Tran, H. T. Le, D. C. Nguyen, H. V. Hoa, N. H. Kim and J. H. Lee, *Prog. Mater. Sci.*, 2021, **117**, 100733.

20 X. Guo, X. Xie, S. Choi, Y. Zhao, H. Liu, C. Wang, S. Chang and G. Wang, *J. Mater. Chem. A*, 2017, **5**, 12445–12452.

21 J. Nan, X. Guo, J. Xiao, X. Li, W. Chen, W. Wu, H. Liu, Y. Wang, M. Wu and G. Wang, *Small*, 2021, **17**, e1902085.

22 J. Halim, M. R. Lukatskaya, K. M. Cook, J. Lu, C. R. Smith, L. A. Naslund, S. J. May, L. Hultman, Y. Gogotsi, P. Eklund and M. W. Barsoum, *Chem. Mater.*, 2014, **26**, 2374–2381.

23 M. Ashton, R. G. Hennig and S. B. Sinnott, *Appl. Phys. Lett.*, 2016, **108**, 023901.

24 D. Sun, M. Wang, Z. Li, G. Fan, L.-Z. Fan and A. Zhou, *Electrochem. Commun.*, 2014, **47**, 80–83.

25 X. Wu, Z. Wang, M. Yu, L. Xiu and J. Qiu, *Adv. Mater.*, 2017, **29**, 1607017.

26 W. Z. Bao, D. W. Su, W. X. Zhang, X. Guo and G. X. Wang, *Adv. Funct. Mater.*, 2016, **26**, 8746–8756.

27 Y. Liu, W. Wang, Y. Ying, Y. Wang and X. Peng, *Dalton Trans.*, 2015, **44**, 7123–7126.

28 A. Byeon, A. M. Glushenkov, B. Anasori, P. Urbankowski, J. W. Li, B. W. Byles, B. Blake, K. L. Van Aken, S. Kota, E. Pomerantseva, J. W. Lee, Y. Chen and Y. Gogotsi, *J. Power Sources*, 2016, **326**, 686–694.

29 S. L. Zhang, X. F. Lu, Z. P. Wu, D. Luan and X. W. D. Lou, *Angew. Chem., Int. Ed. Engl.*, 2021, **60**, 19068–19073.

30 X. Zhou, L. Yu, X.-Y. Yu and X. W. D. Lou, *Adv. Energy Mater.*, 2016, **6**, 201601177.

31 E. Gu, S. Liu, Z. Zhang, Y. Fang, X. Zhou and J. Bao, *J. Alloys Compd.*, 2018, **767**, 131–140.

32 J. Luo, W. Zhang, H. Yuan, C. Jin, L. Zhang, H. Huang, C. Liang, Y. Xia, J. Zhang, Y. Gan and X. Tao, *ACS Nano*, 2017, **11**, 2459–2469.

33 Z. Ma, X. Zhou, W. Deng, D. Lei and Z. Liu, *ACS Appl. Mater. Interfaces*, 2018, **10**, 3634–3643.

34 M. Zhu, Y. Yue, Y. Cheng, Y. Zhang, J. Su, F. Long, X. Jiang, Y. Ma and Y. Gao, *Adv. Electron. Mater.*, 2019, **6**, 1901064.

35 J. Xu, E. Gu, Z. Zhang, Z. Xu, Y. Xu, Y. Du, X. Zhu and X. Zhou, *J. Colloid Interface Sci.*, 2020, **567**, 84–91.

36 Y. Liu, Y. Fang, Z. Zhao, C. Yuan and X. W. D. Lou, *Adv. Energy Mater.*, 2019, **9**, 201803052.

37 Y. Fang, X. Xu, Y. Du, X. Zhu, X. Zhou and J. Bao, *J. Mater. Chem. A*, 2018, **6**, 11244–11251.

38 G. Gao, H. B. Wu, B. Dong, S. Ding and X. W. Lou, *Adv. Sci.*, 2015, **2**, 1400014.

39 M. Q. Zhao, X. Xie, C. E. Ren, T. Makaryan, B. Anasori, G. Wang and Y. Gogotsi, *Adv. Mater.*, 2017, **29**, 1702410.

40 Q. Zhao, Q. Zhu, J. Miao, P. Zhang, P. Wan, L. He and B. Xu, *Small*, 2019, **15**, 1904293.

41 Z. Wu, T. Shang, Y. Deng, Y. Tao and Q. H. Yang, *Adv. Sci.*, 2020, **7**, 1903077.

42 L. Xiu, Z. Wang, M. Yu, X. Wu and J. Qiu, *ACS Nano*, 2018, **12**, 8017–8028.

43 K. Li, X. Wang, S. Li, P. Urbankowski, J. Li, Y. Xu and Y. Gogotsi, *Small*, 2020, **16**, 1906851.

44 L. Jiang and Z. Fan, *Nanoscale*, 2014, **6**, 1922–1945.

45 W. Deng, Q. Fang, H. Huang, X. Zhou, J. Ma and Z. Liu, *Small*, 2017, **13**, 1701231.

46 H. Y. Li, Y. Hou, F. X. Wang, M. R. Lohe, X. D. Zhuang, L. Niu and X. L. Feng, *Adv. Energy Mater.*, 2017, **7**, 1601847.

47 Q. Liu, Y. Li, S. Shen, Z. Zhou, B. Ou and S. Tang, *J. Macromol. Sci., Part A: Pure Appl.Chem.*, 2011, **48**, 518–525.

48 S. Xu, Y. Dall'Agnese, J. Li, Y. Gogotsi and W. Han, *Chem*, 2018, **24**, 18556–18563.

49 Y. X. Yu, *J. Phys. Chem. C*, 2016, **120**, 5288–5296.

50 Y. Zheng, T. Zhou, X. Zhao, W. K. Pang, H. Gao, S. Li, Z. Zhou, H. Liu and Z. Guo, *Adv. Mater.*, 2017, **29**, 1700396.

51 F. Yang, H. Gao, J. Hao, S. Zhang, P. Li, Y. Liu, J. Chen and Z. Guo, *Adv. Funct. Mater.*, 2019, **29**, 1808291.

52 Y. Liu, Z. Tai, T. Zhou, V. Sencadas, J. Zhang, L. Zhang, K. Konstantinov, Z. Guo and H. K. Liu, *Adv. Mater.*, 2017, **29**, 1703028.

53 Z. Y. Lin, D. F. Sun, Q. Huang, J. Yang, M. W. Barsoum and X. B. Yan, *J. Mater. Chem. A*, 2015, **3**, 14096–14100.

54 F. Du, H. Tang, L. M. Pan, T. Zhang, H. M. Lu, J. Xiong, J. Yang and C. Zhang, *Electrochim. Acta*, 2017, **235**, 690–699.

55 J. Song, X. Guo, J. Zhang, Y. Chen, C. Zhang, L. Luo, F. Wang and G. Wang, *J. Mater. Chem. A*, 2019, **7**, 6507–6513.

56 Y. Z. Fang, R. Hu, B. Y. Liu, Y. Y. Zhang, K. Zhu, J. Yan, K. Ye, K. Cheng, G. L. Wang and D. X. Cao, *J. Mater. Chem. A*, 2019, **7**, 5363–5372.

This journal is © The Royal Society of Chemistry 2021

J. Mater. Chem. A, 2021, **9**, 23841–23849 | **23849**